Chinese Chemical Letters 36 (2025) 109873

Contents lists available at ScienceDirect

Chinese Chemical Letters

journal homepage: www.elsevier.com/locate/cclet

Molybdenum-glycerate@zeolitic imidazolate framework spheres derived hierarchical nitrogen-doped carbon-encapsulated bimetallic selenides heterostructures for improved lithium-ion storage

Ming Zhong[a,c,*], Xue Guo[a], Yang Liu[a], Kun Zhao[a], Hui Peng[c], Suijun Liu[b,*], Xiaobo Zhang[a,*]

[a] State Key Laboratory of Advanced Processing and Recycling of Nonferrous Metals, Lanzhou University of Technology, Lanzhou 730050, China
[b] School of Chemistry and Chemical Engineering, Jiangxi Provincial Key Laboratory of Functional Molecular Materials Chemistry, Jiangxi University of Science and Technology, Ganzhou 341000, China
[c] Key Laboratory of Eco-Functional Polymer Materials of the Ministry of Education, Key Laboratory of Eco-Environmental Polymer Materials of Gansu Province, College of Chemistry and Chemical Engineering, Northwest Normal University, Lanzhou 730070, China

ARTICLE INFO

Article history:
Received 7 February 2024
Revised 24 March 2024
Accepted 8 April 2024
Available online 10 April 2024

Keywords:
Zeolitic imidazolate framework
Heterostructure
Core-shell structure
Electrode material
Lithium-ion battery

ABSTRACT

In this work, the synthesis of uniform zeolitic imidazolate framework-coated Mo-glycerate spheres and their subsequent conversion into hierarchical architecture containing bimetallic selenides heterostructures and nitrogen-doped carbon shell are reported. Selenization temperature plays a significant role in determining the phases, morphology, and lithium-ion storage performance of the composite. Notably, the optimal electrode demonstrates an ultrahigh reversible capacity of 1298.2 mAh/g after 100 cycles at 0.2 A/g and an outstanding rate capability with the capacity still maintained 505.7 mAh/g after 300 cycles at 1.0 A/g, surpassing the calculated theoretical capacity according to individual component and most of the reported MoSe@C- or ZnSe@C-based anodes. Furthermore, *ex-situ* X-ray diffraction patterns reveal the combined conversion and alloying reaction mechanisms of the composite.

The widespread adoption of electric vehicles and portable electronic devices has highlighted the immense potential of lithium-ion batteries (LIBs) as a power source. Unfortunately, the current commercial graphite-type carbon anodes are unable to meet the growing market demands due to their inherently low theoretical capacity [1–5]. To achieve exceptional comprehensive performances, transition-metal chalcogenides, particularly selenides, have garnered significant interest for their high theoretical capacities (over 600 mAh/g), excellent electrical conductivity, and abundant redox chemistry [6]. However, transition-metal selenides face challenges such as severe volume expansion/shrinkage and particle aggregation. Therefore, it is of utmost importance to explore alternative strategies to address these issues [7,8].

As an illustrative case, the construction of carbon-encapsulated metal selenide composites has been shown to accelerate electron transfer, ensure structural integrity, and enhance the specific capacity of metal selenides [9,10]. Additionally, numerous endeavors have been undertaken to further augment the performance of lithium-ion storage, including the construction of heterostructures [11,12], the introduction of defects, and the implementation of nano architectures [13,14]. Among these, heterostructures are considered a promising avenue due to the interface effect and built-in potential generated at the hetero-interface, which contribute to low activation energy and rapid ion/electron transfer and diffusion kinetics, ultimately leading to improved lithium-ion storage performance [15–19].

With these advantages in mind, we intelligently fabricated a series of N-doped carbon-encapsulated bimetallic selenides heterostructure composites ($MoSe_2$/ZnSe@NC) through the selenization of zeolitic imidazolate framework (ZIF) coated Mo-glycerate (MOG) precursor at varying temperatures. Typical synthesis procedure is presented in Fig. 1a. Initially, MOG was prepared through a solvothermal reaction utilizing $MoO_2(acac)_2$ as a Mo source. Scanning electron microscopy (SEM) verifies its regular spherical feature with a smooth surface (Fig. 1b). X-ray diffraction (XRD) pattern matches well with the results reported elsewhere (Fig. S1 in Supporting information) [20]. The core-shell MOG@ZIF-8 precursors were *in situ* obtained by mixing the methanol solution containing $Zn(NO_3)_2{\cdot}6H_2O$ and 2-MeIM with the MOG dispersion. The XRD pattern reveals that the characteristic peaks of MOG@ZIF8 highly coincide with the standard card or the fitted pattern, with

* Corresponding authors.
E-mail addresses: zhongming@lut.edu.cn (M. Zhong), sjliu@jxust.edu.cn (S. Liu), xbzhang@lut.edu.cn (X. Zhang).

https://doi.org/10.1016/j.cclet.2024.109873
1001-8417/

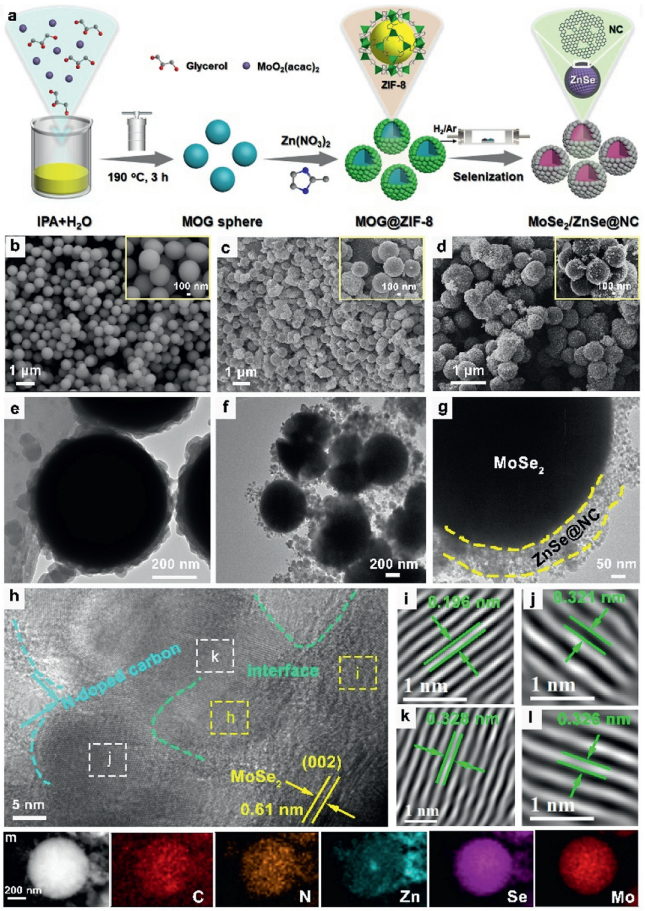

Fig. 1. (a) Schematic preparation of the $MoSe_2$/ZnSe@NC composites. Morphology and microstructure characterizations: different magnified SEM images of (b) MOG, (c) MOG@ZIF-8 precursor, and (d) $MoSe_2$/ZnSe@NC-700. (e) TEM image of MOG@ZIF-8. (f-l) Different-magnified TEM images of $MoSe_2$/ZnSe@NC-700. (m) HAADF-STEM and corresponding elemental mappings of $MoSe_2$/ZnSe@NC-700.

no miscellaneous peaks appearing. This indicates the successful preparation of the precursor (Fig. S2 in Supporting information). Furthermore, the morphology of MOG@ZIF-8 was examined through SEM and transmission electron microscopy (TEM) (Figs. 1c and e), which reveal ZIF-8 nanoparticles are densely adhered to the surface of MOG, resulting in a distinct core-shell architecture with a rough surface. Ultimately, the $MoSe_2$/ZnSe@NC composite was synthesized *via* direct selenization of the MOG@ZIF-8 precursor under a reduced atmosphere. According to the TG curve result of MOG@ZIF-8 (Fig. S3 in Supporting information), the selenization temperature was primarily set at 600, 700, and 800 °C, aiming to investigate the impact of temperature on the configuration, composition, and battery performance of the final composites.

The SEM images show that the composites obtained at 600 and 700 °C exhibit a well-preserved macroscopic morphology with minimal aggregation (Fig. 1d and Fig. S4a in Supporting information). In contrast, the composite obtained at 800 °C displays an irregular and agglomerated block topography (Fig. S4b in Supporting information). Furthermore, the low-magnified TEM image reveals a core-shell morphology of the $MoSe_2$/ZnSe@NC composite consistent with the SEM results (Figs. 1f and g). The high-resolution TEM image shows that carbon is uniformly coated on the surface of ZnSe, and they are also attached to the $MoSe_2$ spheres as a whole (Fig. 1h). Besides, clear heterostructure interfaces are observed between ZnSe and $MoSe_2$ phases, which is beneficial for the formation of built-in potential at the hetero-interface to accelerate charge transport and increase the ion/electron transfer rate of the composite during battery operation [21]. The lattice fringe space of 0.61 nm matches well with the (002) plane of $MoSe_2$, providing strong evidence for the conversion of MOG to $MoSe_2$. The lattice fringe spaces of 0.196 and 0.321 nm are assigned to the (105) and (004) planes of $MoSe_2$, respectively (Figs. 1i and j). Meanwhile, both lattice fringes of 0.328 and 0.326 nm correspond to the (111) plane of ZnSe (Figs. 1k and l). Elemental mapping reveals that C, N, Zn, Se, and Mo elements are uniformly distributed in the $MoSe_2$/ZnSe@NC composite (Fig. 1m).

Fig. 2a shows the diffraction peaks of the composites after selenization, which are all well-matched with the diffraction peaks on the standard $MoSe_2$ (JCPDS No. 17-887) and ZnSe (JCPDS No. 01–690). In contrast to $MoSe_2$/ZnSe@NC-600 and −800, the diffraction peaks of $MoSe_2$/ZnSe@NC-700 show the narrowest half-peak widths, the strongest peaks, and the best crystallinity. During selenization, Se powders are reduced to Se^{2-} anions under a reduced atmosphere, which then react with zinc ions from ZIF-8 and molybdenum ions from MOG to generate ZnSe and $MoSe_2$, respectively ($Zn^{2+} + Se^{2-} \rightarrow ZnSe$, $Mo^{4+} + Se^{2-} \rightarrow MoSe_2$). The presence of carbon in $MoSe_2$/ZnSe@NC is verified by Raman spectroscopy. The I_D/I_G value of $MoSe_2$/ZnSe@NC-800 (1.05) is lower than that of $MoSe_2$/ZnSe@NC-600 (1.13) and $MoSe_2$/ZnSe@NC-700 (1.15), indicating a higher graphitization degree and superior electrical conductivity of carbon (Fig. 2b). Additionally, the typical 2D peak at 2867 cm^{-1} suggests that carbon is graphitized, thereby providing good electrical conductivity for the composite.

The composition and chemical valences of various elements in $MoSe_2$/ZnSe@NC-700 were analyzed using X-ray photoelectron spectroscopy (XPS). The survey spectrum confirms the presence of Mo, Zn, Se, C, and N elements in the composite (Fig. S5 in Supporting information). In the Mo 3d spectrum (Fig. 2c), the peaks at 229.5 and 232.4 eV are identified as typical Mo^{4+} ($3d_{3/2}$) and Mo^{4+} ($3d_{5/2}$), respectively, while the peaks observed at 230.4 and 233.0 eV are attributed to Mo^{6+} ($3d_{3/2}$) and Mo^{6+} ($3d_{5/2}$), respectively [22]. The Zn 2p spectrum of ZIF-8 derived ZnSe@NC shows a binding energy of 23.1 eV between two peaks, which confirms the existence of Zn^{2+} (Fig. 2d) [23]. In comparison, the corresponding peaks of the Zn 2p spectrum for $MoSe_2$/ZnSe@NC shift towards lower binding energies, indicating the existence of interaction between ZnSe and $MoSe_2$ phases induced by the heterostructure interface. The high-resolution Se 3d spectrum contains two main peaks at 52.9 eV (Se $3d_{5/2}$) and 54.1 eV (Se $3d_{3/2}$) (Fig. 2e), indicating the existence of Se^{2+} in $MoSe_2$/ZnSe@NC [24]. The C 1s spectrum displays three divided peaks at 284.6, 286.3, and 288.5 eV (Fig. 2f), which are attributed to C=C, C–N, and C=O bonds, respectively [25]. Furthermore, the N 1s spectrum can be segregated into two distinct peaks at 396.2 and 398.1 eV, which correspond to pyridinic N and pyrrolic N, respectively (Fig. 2g). Other two small peaks with binding energies of 400.9 and 403.2 eV are assigned to graphitic N and oxidized type N-functionalities, respectively [26]. Moreover, nitrogen adsorption-desorption isotherms confirm that $MoSe_2$/ZnSe@NC-700 exhibits a larger BET specific surface area (54.22 m^2/g) and pore size (14 nm) than $MoSe_2$/ZnSe@NC-600 (24.19 m^2/g, 11 nm) and $MoSe_2$/ZnSe@NC-800 (24.19 m^2/g, 10 nm), indicating its more exposed active species, faster electrolyte permeation, and superior electrochemical performance (Fig. 2h and Fig. S6 in Supporting information).

The electrochemical performance of the $MoSe_2$/ZnSe@NC composites are initially examined through cyclic voltammetry (CV) curves (Fig. 3a). During the first cathodic process, a broad peak ranging from 0.23 V to 0.87 V is assigned to the generation of solid-electrolyte-interface (SEI) film and the conversion reactions of $MoSe_2$ and ZnSe with Li^+ ions to produce metallic Mo, Zn, and Li_2Se products [27]. Additionally, a small peak at 0.18 V is attributed to the multi-step alloying reaction between Zn and Li to form various Li_yZn alloys ($LiZn_2$, $LiZn_4$, Li_2Zn_3, LiZn, *etc.*) [28]. In the initial anodic process, two minor oxidation peaks at 0.53 and

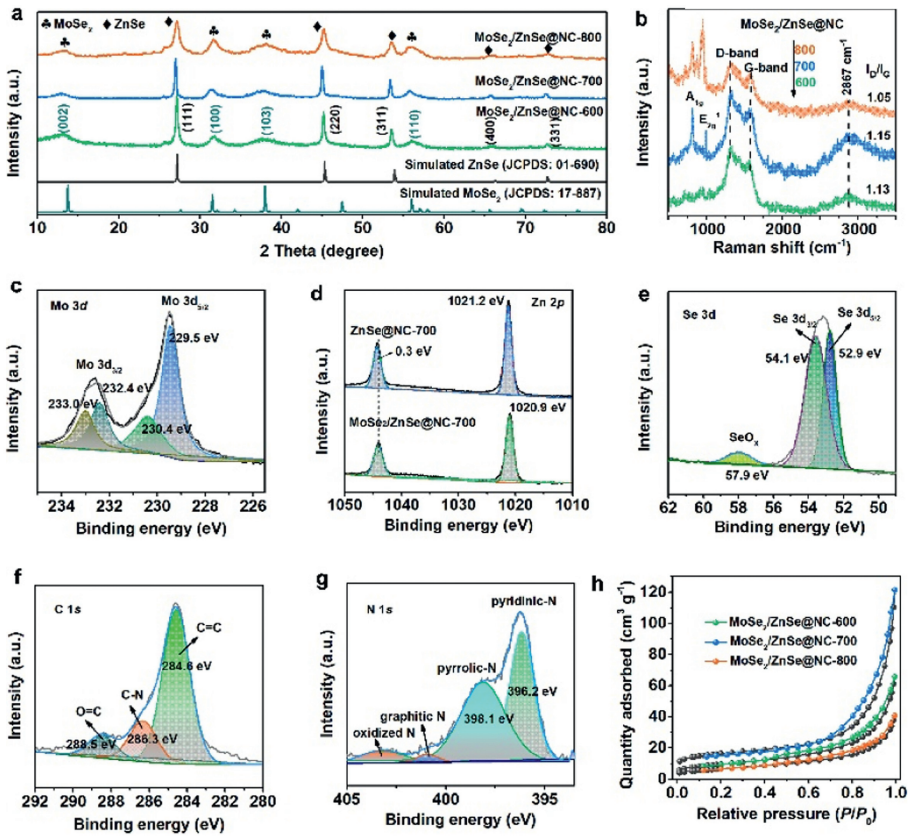

Fig. 2. (a) XRD patterns and (b) Raman spectra of $MoSe_2$/ZnSe@NC-600, −700, and −800. High resolution XPS spectra of $MoSe_2$/ZnSe@NC-700: (c) Mo 3d, (d) Zn 2p, (e) Se 3d, (f) C 1s, and (g) N 1s. (h) N_2 adsorption-desorption isotherms of $MoSe_2$/ZnSe@NC-600, −700, and −800.

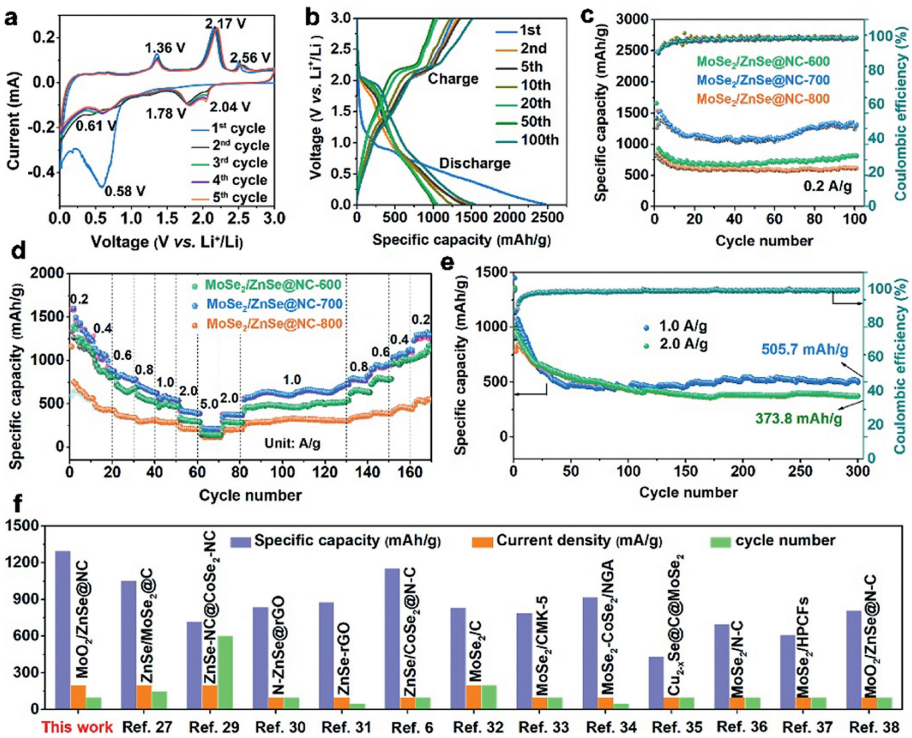

Fig. 3. (a) CV curves and (b) voltage-capacitance curves of $MoSe_2$/ZnSe@NC-700. (c) Cycling performance of $MoSe_2$/ZnSe@NC at 0.2 A/g. (d) Rate capabilities of $MoSe_2$/ZnSe@NC from 0.2 A/g to 5.0 A/g. (e) Long-term stabilities of $MoSe_2$/ZnSe@NC-700. (f) Performance comparison of $MoSe_2$/ZnSe@NC-700 with reported $MoSe_2$- and ZnSe-based anodes.

0.68 V correspond to the multi-step dealloying process of Li_yZn alloys. The other two prominent peaks at 1.36 and 2.56 V are assigned to the oxidation of Zn and Li_2Se into ZnSe [27], while the oxidation peak at 2.17 V demonstrates the conversion of Mo to $MoSe_2$ [26]. In subsequent cycles, the CV curves overlap, indicating excellent cycling stability for the $MoSe_2$/ZnSe@NC electrode. The voltage-capacitance curves of $MoSe_2$/ZnSe@NC-700 at 200 mA/g reveal that the first discharge and charge capacities are 2496.2 and 1255.7 mAh/g, respectively (Fig. 3b). The capacity decay may be attributed to the decomposition of electrolytes and the formation of SEI film. In subsequent cycles, the specific capacities maintain above 1000 mAh/g, further indicating its exceptional reversibility for Li^+ ion storage.

The cycling performances of the $MoSe_2$/ZnSe@NC electrodes at a current density of 0.2 A/g are shown in Fig. 3c. It is noteworthy that all of the composites exhibit Coulombic efficiencies of nearly 99%, indicating their excellent cyclic stabilities. After 100 cycles, $MoSe_2$/ZnSe@NC-700 delivers the highest specific capacity up to 1298.2 mAh/g than $MoSe_2$/ZnSe@NC-600 and −800, which show the capacities of 822.9 and 620.3 mAh/g, respectively. The observed increase in capacity during cycling may be attributed to the activation of electrode materials and the reversible formation/dissolution of a conducting-type polymeric film at low potential in an alkyl carbonate solution. Furthermore, SEM and TEM images of the $MoSe_2/MoO_2$@C-700 electrode after repeated discharge-charge cycles confirm the preservation of a spherical and core-shelled morphology similar to the pristine one (Fig. S7 in Supporting information). So under 700 °C, individual MOG-derived $MoSe_2/MoO_2$@C-700 and ZIF-8-derived ZnSe@NC-700, evidenced by XRD patterns (Figs. S8 and S9 in Supporting information), were prepared for performance comparison. ZnSe@NC-700 and $MoSe_2/MoO_2$@C-700 exhibit much lower capacities compared to $MoSe_2$/ZnSe@NC-700 (Fig. S10 in Supporting information), highlighting the structural and component advantages of $MoSe_2$/ZnSe@NC in improving the lithium-ion storage performance.

Fig. 3d illustrates the rate performances of the $MoSe_2$/ZnSe@NC composites. As observed, $MoSe_2$/ZnSe@NC-700 exhibits superior rate capability compared to $MoSe_2$/ZnSe@NC-600 and −800. As the current density increases from 0.2 A/g to 0.4, 0.6, 0.8, 1.0, 2.0, and 5.0 A/g, the discharge capacities of $MoSe_2$/ZnSe@NC-700 are 1347.7, 1079.0, 815.5, 683.7, 585.5, 411.3, and 227.4 mAh/g, respectively. When the current density is restored to 1.0 A/g, its reversible capacity after 50 cycles still maintains 721.7 mAh/g, and the capacity recovers 1293.1 mAh/g with further increasing the current density to 0.2 A/g, almost no capacity decay compared with the initial value. At equivalent current densities, the capacities of $MoSe_2$/ZnSe@NC-700 exceed those of $MoSe_2$/ZnSe@NC-600 and −800. This is primarily due to the fact that $MoSe_2$/ZnSe@NC-700 maintains the optimal structure and morphology of the pristine precursor, and exhibits the largest specific surface area compared to $MoSe_2$/ZnSe@NC-600 and −800, which results in an increased contact area between active species and electrolytes, promoting the fast ions/electrons transport and thereby enhancing the electrochemical performance. Additionally, the rate capability of $MoSe_2$/ZnSe@NC-700 surpasses that of MOG-derived $MoSe_2/MoO_2$@C-700 and ZIF-8-derived ZnSe@NC-700 (Fig. S11 in Supporting Information), further confirming that the rational construction of the hierarchical composite is beneficial for achieving outstanding lithium-ion storage performance. Moreover, $MoSe_2$/ZnSe@NC-700 delivers reversible capacities of 505.7 and 378.3 mAh/g after 300 cycles at 1.0 and 2.0 A/g, respectively, indicating excellent cycling stability (Fig. 3e), Additionally, the lithium-ion storage performance surpasses its theoretical capacity calculated according to the inductively coupled plasma (ICP) results (422 mAh/g × 56.19 wt% + 577 mAh/g × 35.38 wt% + 372 mAh/g × 8.43 wt% = 472.2 mAh/g) and other reported molybdenum selenide@carbon- and zinc selenide@carbon-based anodes (Fig. 3f) [6,27,29–38].

Subsequently, electrochemical impedance spectroscopy (EIS) was conducted on three $MoSe_2$/ZnSe@NC electrodes to elucidate their exceptional lithium-ion storage performance. Fig. 4a illustrates that $MoSe_2$/ZnSe@NC-700 exhibits a smaller charge transfer resistance (R_{ct}) of 164.5 Ω compared to $MoSe_2$/ZnSe@NC-600 and −800, which display R_{ct} values of 174.0 and 198.5 Ω, respectively. This may be attributed to $MoSe_2$/ZnSe@NC-700′s superior structural integrity, largest specific surface area, and unique pore structure, which collectively facilitate excellent charge transport. Additionally, the Li^+ ion diffusion coefficient (D_{Li^+}) for $MoSe_2$/ZnSe@NC-700 is calculated to be 3.14 and 5.04 times higher than those of $MoSe_2$/ZnSe@NC-600 and $MoSe_2$/ZnSe@NC-800, respectively, further corroborating a faster Li^+ ion diffusion kinetics in $MoSe_2$/ZnSe@NC-700 (Fig. 4b).

To gain a deeper understanding of the electrochemical reaction kinetics of the optimal $MoSe_2$/ZnSe@NC-700 electrode, CV tests were conducted. All of the CV curves exhibit highly identical shapes (Fig. 4c), indicating the stable electrochemical performance. Three oxidation peaks shift to higher voltages while the reduction peaks move to lower voltages with sweep rate changing from 0.1 mV/s to 1.0 mV/s, indicating an inevitable polarization of the electrode during cycling. By fitting the redox peaks in CV (Fig. 4d) [39,40], the capacitance and diffusion contributions were determined, and the results demonstrate a typical pseudocapacitance-dominant behavior of $MoSe_2$/ZnSe@NC-700. Furthermore, the proportion of pseudocapitance contribution at 0.6 mV/s is about 81.5% (Fig. 4e). Fig. 4f shows the contribution percentage of pseudocapitance at various sweep rates, which find that the redox contribution of pseudocapacitance gradually becomes the dominant component of the total capacitance as the sweep rate increases. The higher contribution of pseudocapitance significantly enhances the electrochemical lithium-ion storage performance.

Fig. 4g displays *ex-situ* XRD patterns for the first cycle at different voltage stages. During the discharge process, two peaks at $2\theta = 11.3°$ and 26.8°, which correspond to $MoSe_2$ and ZnSe phases, respectively, exhibit a gradual decrease and eventually disappear when the battery is discharged to 0.01 V, indicating the occurrence of conversion reactions of ZnSe and $MoSe_2$. Simultaneously, new diffraction peaks gradually emerge at $2\theta = 38.6°$ and 45.3°, representing the formation of Li_2Se and Li_yZn phases. These processes keep pace with the CV results. During subsequent charging, the characteristic diffraction peaks of $MoSe_2$ and ZnSe gradually reappear, while the diffraction peaks representing the Li_2Se and Li_yZn phases disappear, indicating the occurrence of reversible oxidation reactions.

To evaluate a practical application, the full battery was assembled by using $MoSe_2$/ZnSe@NC-700 as the anode and commercial $LiCoO_2$ as the cathode. Results show that the $MoSe_2$/ZnSe@NC-700||$LiCoO_2$ battery exhibits a high voltage of 3.5 V and excellent rate capability with the charging capacities at 0.1, 0.2, 0.4, 0.6, 0.8, 1.0, 2.0 A/g of 153.2, 147.5, 138.9, 127.5, 117.5, 108.1, and 78.8 mAh/g (Fig. S12 in Supporting information), showing good capacity retention at different current densities.

In conclusion, this work successfully synthesized hierarchical $MoSe_2$/ZnSe@NC composites. Various characterizations have confirmed the unique core-shell structure, $MoSe_2$/ZnSe heterostructure, and N-doped carbon-coating collectively endow the composite with ultrahigh reversible capacity, outstanding rate performance, and cyclicity. Moreover, *ex-situ* PXRD patterns have revealed the coexistence of conversion and alloying reaction processes. It is believed that the innovative synthesis of $MoSe_2$/ZnSe@NC can serve as a model for designing and constructing core-shell heterostructure-based composites with exceptional lithium-ion storage performance.

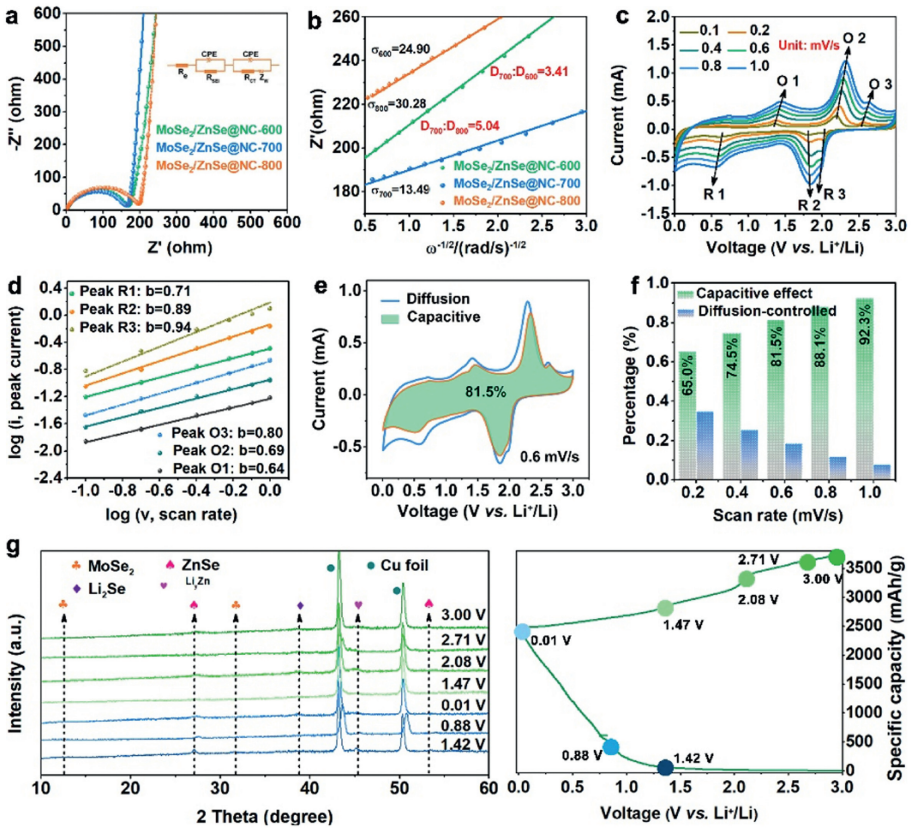

Fig. 4. (a) Nyquist plots of $MoSe_2$/ZnSe@NC-600, −700, and −800. (b) Plots of Z' *versus* $\omega^{-1/2}$. (c) CV curves at different sweep rates. (d) log(i)-log(v) plots. (e) Proportion of capacitance at 0.6 mV/s. (f) Percentages of capacitance and diffusion contributions. (g) *Ex-situ* XRD patterns of $MoSe_2$/ZnSe@NC-700 at various voltages during the first cycling process.

Declaration of competing interest

The authors declare that they have no known competing financial interests or personal relationships that could have appeared to influence the work reported in this paper.

CRediT authorship contribution statement

Ming Zhong: Conceptualization, Data curation, Funding acquisition, Methodology, Project administration, Supervision. **Xue Guo:** Data curation, Formal analysis, Investigation. **Yang Liu:** Data curation, Investigation. **Kun Zhao:** Data curation, Investigation. **Hui Peng:** Data curation, Investigation. **Suijun Liu:** Project administration. **Xiaobo Zhang:** Project administration, Supervision.

Acknowledgments

This work was financially supported by the National Natural Science Foundation of China (No. 22265017) and the Open Fund of Key Laboratory of Eco-functional Polymer Materials of the Ministry of Education (No. KF-21-04).

Supplementary materials

Supplementary material associated with this article can be found, in the online version, at doi:10.1016/j.cclet.2024.109873.

References

[1] P. Luo, C. Zheng, J. He, Adv. Funct. Mater. 32 (2022) 2107277.
[2] L. Zhao, B. Ding, X.Y. Qin, Adv. Mater. 34 (2022) 2106704.
[3] Y. Tong, Y. Wu, Z. Liu, Chin. Chem. Lett. 34 (2023) 107443.
[4] J. Zheng, Y. Sun, Y. Wu, J. Power Sources 492 (2021) 229614.
[5] Q. Zhang, B. Xi, W. Chen, Nano Res. 15 (2022) 6184–6191.
[6] Q. Liu, J. Hou, Q. Hao, Nanoscale 12 (2020) 22778–22786.
[7] X. Guo, J. Zhang, L. Yuan, Adv. Energy Mater. 13 (2023) 2204376.
[8] Y. Wu, Y. Sun, J. Zheng, J. Phys. Energy 3 (2021) 032009.
[9] S.Q. Zhang, Z.H. Wang, X.J. Hu, J. Alloys Compds. 863 (2021) 158329.
[10] W. Tian, W. Ma, Z. Feng, J. Energy Chem. 44 (2020) 97–105.
[11] H. Fu, Q. Wen, P.Y. Li, Small Methods 6 (2022) 2201025.
[12] X. Liu, Y. Tong, Y. Wu, Small Methods 5 (2021) 2101130.
[13] J.R. Shang, H.L. Dong, H.B. Geng, Nanoscale 12 (2020) 23645–23652.
[14] Y.Y. Liu, M. Zhong, L.J. Kong, Inorg. Chem. Front. 6 (2019) 50–56.
[15] H. Liu, W. Zhang, W. Wang, Small 19 (2023) 2304264.
[16] X. Liu, Z. Sun, Y. Sun, Adv. Funct. Mater. 33 (2023) 2307205.
[17] Y. Chu, L. Guo, B. Xi, Adv. Mater. 30 (2018) 1704244.
[18] Z. Chen, Y. Wu, X. Liu, J. Energy Chem. 81 (2023) 462–471.
[19] X. Liu, Y. Sun, Y. Tong, H. Li, Small 18 (2022) 2204045.
[20] Y. Wang, L. Yu, X.W. Lou, Angew. Chem. 128 (2016) 7549–7552.
[21] A.K. Kakarla, H. Bandi, R. Shanthappa, J.S. Yu, Small Methods 7 (2023) 2201315.
[22] Y.N. Xu, X.F. Liu, H. Su, Energy Environ. Mater. 5 (2022) 627–636.
[23] M. Zhong, Y. Lin, B. Yue, New J. Chem. 46 (2022) 14346–14352.
[24] X. Li, Z. Han, W. Yang, Adv. Funct. Mater. 31 (2021) 2106194.
[25] F. He, Y. Han, Y. Tong, ACS Sustain. Chem. Eng. 10 (2022) 6094–6105.
[26] Q. Liang, L. Zhang, M. Zhang, ACS Sustain. Chem. Eng. 8 (2020) 14127–14136.
[27] L. Zeng, Y. Fang, L. Xu, Nanoscale 11 (2019) 6766–6775.
[28] Z. Cao, J. Cui, D. Yu, Adv. Funct. Mater. 33 (2023) 2306862.
[29] X. Hu, X. Liu, K. Chen, G. Wang, H. Wang, J. Mater. Chem. A 7 (2019) 11016–11037.
[30] X. Liu, Y. Liu, M. Feng, L.Z. Fan, J. Mater. Chem. A 6 (2018) 23621–23627.
[31] Z. Zhang, Y. Fu, X. Yang, Y. Qu, Q. Li, Electrochim. Acta 168 (2015) 285–291.
[32] Q. Su, X. Cao, X. Kong, Electrochim. Acta 292 (2018) 339–346.
[33] C. Zheng, C. Chen, L. Chen, M. Wei, J. Mater. Chem. A 5 (2017) 19632–19638.
[34] X. Zhang, J. Zhou, Y. Zheng, D. Chen, J. Power Sources 439 (2019) 227112.
[35] R. Jin, X. Liu, L. Yang, G. Li, S. Gao, Electrochim. Acta 259 (2018) 841–849.
[36] W. Tang, D. Xie, T. Shen, Chem. Eur. J. 23 (2017) 12924–12929.
[37] M. Zhu, Z. Luo, A. Pan, Chem. Eng. J. 334 (2018) 2190–2200.
[38] M. Zhong, L. Li, K. Zhao, New J. Chem. 45 (2021) 12064–12070.
[39] M. Zhong, X. Guo, L. Li, ACS Appl. Nano Mater. 6 (2023) 20018–20027.
[40] Y. Sun, J. Zheng, Y. Yang, Compos. Commun. 24 (2021) 100674.